Materials Transactions, Vol. 60, No. 8 (2019) pp. 1533 to 1542
Special Issue on Severe Plastic Deformation for Nanomaterials with Advanced Functionality

The Development of Vacancies during Severe Plastic Deformation

J. Čížek[1,*], M. Janeček[2], T. Vlasák[1], B. Smola[2], O. Melikhova[1], R.K. Islamgaliev[3] and S.V. Dobatkin[4]

[1]*Faculty of Mathematics and Physics, Charles University in Prague, Department of Low Temperature Physics, V Holešovičkách 2, Prague 8, CZ-18000, Czech Republic*
[2]*Faculty of Mathematics and Physics, Charles University in Prague, Department of Physics of Materials, Ke Karlovu 5, 12116 Prague 2, CZ-12116, Czech Republic*
[3]*Institute of Physics of Advanced Materials, Ufa State Aviation Technical University, 12 K. Marx Street, 450000 Ufa, Russia*
[4]*A.A. Baikov Institute of Metallurgy and Materials Science, Russian Academy of Sciences, Moscow, Russia*

A high density of lattice defects is introduced to materials by severe plastic deformation (SPD). Numerous experimental techniques, in particular electron microscopy, X-ray, electron and neutron diffraction, etc. are employed to characterize the evolution of microstructure and defects with strain introduced to the material by SPD. These techniques concentrate mainly on the investigation of planar (grain boundaries) and line defects (dislocations). On the other hand, point defects, namely vacancies and their agglomerates are investigated in less detail. Positron annihilation spectroscopy (PAS) proved to be an effective method for the investigation of point defects and dislocations in ultra-fine grained (UFG) materials. This study summarizes the results of the investigation of lattice defects in UFG metals with fcc (Al, Ni, Cu), bcc (Fe, Nb, W) and hcp (Mg, Ti) structure prepared by high pressure torsion (HPT). Two techniques of PAS were employed (i) positron lifetime spectroscopy (LT) allowing to characterize the type and concentration ratio of lattice defects in the severely deformed material and (ii) Doppler broadening (DB) of annihilation radiation providing analysis of the homogeneity of the UFG structure and spatial distribution of defects. The latter technique was complemented by mapping of microhardness distribution throughout the surface of the HPT specimens.

The LT studies revealed that HPT straining at room temperature introduced not only dislocations but also a high concentration of vacancies. A significant fraction of deformation-induced vacancies disappeared by diffusion to sinks at grain boundaries. Remaining vacancies agglomerated into vacancy clusters. The average size of vacancy clusters differs in various metals and is affected by the activation energy for migration of vacancies in the given material.

The analysis of DB of positron annihilation radiation and its correlation with microhardness distribution indicated that dislocation density tends to saturate with strain. On the other hand, the spatial (lateral) distribution of vacancy clusters remains non-uniform even in samples subjected to a high number of HPT revolutions. The average size of vacancy clusters increases with radial distance from the centre of the sample due to the increasing production rate of vacancies. [doi:10.2320/matertrans.MF201937]

(Received March 1, 2019; Accepted May 23, 2019; Published July 25, 2019)

Keywords: *severe plastic deformation, vacancies, positron annihilation spectroscopy*

1. Introduction

Severe plastic deformation (SPD) enables to achieve extremely strong grain refinement of polycrystalline materials down to nanoscale.[1)] Repeated application of SPD results in production of bulk ultra fine-grained (UFG) materials with grain size typically in the range 100–500 nm.[2)] A number of advanced SPD techniques has been developed.[2,3)] The strongest grain refinement is usually achieved by high pressure torsion (HPT).[4–6)] Due to this reason, HPT was used as the sample processing method in the present work. In HPT processing a disk sample is pressed between two anvils by a high pressure of severe GPa and simultaneously repeatedly strained by rotating one of the anvil.[2,4–6)] The strain imposed to the sample during HPT processing is not uniform but increases from the centre of the sample towards the periphery.[2,4–6)] The shear strain of a sample subjected to N HPT revolutions can be estimated from the relation[2)]

$$\gamma = \frac{2\pi r N}{h}, \tag{1}$$

where h is the thickness of the deformed sample and r is the radial distance from the centre of the sample disk corresponding to the rotation axis. The non-uniform radial distribution of strain across the sample affects the homogeneity of UFG structure of samples prepared by HPT. This issue has been extensively studied in the recent years.[7–11)] In most materials the strengthening measured usually by microhardness in regions with equal γ is comparable.[5,12–14)] Hence, samples subjected to various numbers N of HPT revolutions exhibit comparable hardness in such distances r from the centre where eq. (1) gives the same value of strain γ. The radial variation of strain according to eq. (1) can be also utilized for the examination of the effect of strain magnitude on the UFG microstructure by examining a HPT deformed sample in various distances r from the centre.

The UFG structure is characterized not only by very small grain size, but also by a high concentration of lattice defects. The fine grain structure contains a high volume fraction of grain boundaries. Moreover, the SPD processing introduces a high density of dislocations and also vacancies which are created by a non-conservative motion of dislocations, e.g. the dislocation climbing. Lattice defects introduced by SPD are crucial for unique properties of UFG materials. Hence, investigation of lattice defects in UFG materials and their development during SPD processing is very important for understanding the exceptional physical properties of UFG materials. For example, enhanced self-diffusion[2)] and diffusivity of solutes reported for UFG materials[15,16)] is related not only to a significant volume fraction of grain boundaries providing additional pathways for diffusion but also to a high concentration of vacancies introduced by SPD. Contrary to dislocations which can be observed directly by transmission electron microscopy (TEM) investigations of vacancies is more difficult.

*Corresponding author, E-mail: jakub.cizek@mff.cuni.cz

Deformation-induced vacancies can be detected through measurement of the total stored deformation energy using electrical resistometry[17] or differential scanning calorimetry (DSC).[18] Recovery of deformation-induced defects (vacancies and dislocations) during annealing of the sample can be observed as drops of residual electrical resistivity and as exothermic peaks in DSC heating curves.[18,19] Typically vacancies are annealed at lower temperatures than dislocations so the peak which can be attributed to recovery of vacancies precedes the peak caused by annealing of dislocations. The areas of DSC peaks correspond to the total enthalpy of defect annealing.[18] If the formation enthalpy of vacancies is known vacancy concentration can be determined from the stored deformation energy corresponding to the vacancy annealing peak in DSC curve. The net concentration of vacancies in HPT deformed Ni[18] and steel[20] samples determined from the area of the exothermic DSC peaks attributed to recovery of vacancies was in the order of magnitude of $\sim 10^{-4}$. Similar concentration of vacancies was estimated in HPT deformed Ni also by electrical resistometry.[18] This value is close to the equilibrium concentration of vacancies in Ni close to the melting temperature.

Another approach which does not require the knowledge about the vacancy formation enthalpy is comparison of electrical resistometry or DSC with X-ray line profile analysis (XLPA).[21] The total stored energy measured by electrical resistometry or DSC contain contribution from both vacancies and dislocations. However, in contrast to dislocations, vacancies do not contribute to broadening of X-ray profiles but cause diffuse scattering only.[21] The mean dislocation densities in UFG Cu estimated from the deformation stored energy measured by DSC and residual electrical resistivity were three to four times higher than those obtained XLPA.[21] This discrepancy is due to excess vacancies, which also contribute to the total stored energy but not to broadening of X-ray line profiles. This was further supported by a small shift of centroids of X-ray diffraction (XRD) peaks to higher scattering angles in Cu samples deformed by SPD.[22] Such shift of XRD peaks indicates the shrinkage of lattice which is consistent with the presence of relaxed vacancies and/or vacancy clusters. The concentration of vacancies introduced by SPD into Cu was estimated by DSC combined with XLPA to fall into the range of 10^{-4}–10^{-3} at.$^{-1}$ which is comparable to the vacancy concentrations close to the melting point of copper.[21] Hence, both electrical resistometry and DSC provide indirect indications that very high concentration of vacancies is created by SPD straining.[21–24]

The concentration of deformation-induced vacancies can be determined also by dilatometry.[25] Simultaneous measurement of macroscopic length change $\Delta L/L$ by dilatometry and change of the lattice parameter $\Delta a/a$ by X-ray diffraction enables to determine the concentration of vacancies as $c_v = 1/3(\Delta L/L - \Delta a/a)$.[26] Similarly dilatometry measurements of macroscopic length change $\Delta L/L$ can be combined with electrical resistomery.[27,28] The concentration of deformation-induced vacancies determined using this approach in HPT-deformed Cu is again in the order of magnitude of 10^{-4}.[18]

The absolute concentration of free volumes can be determined also by time dependent differential dilatometry.[29–32] This type of measurement is based on precise determination of macroscopic length change of sample containing open volume defects and defect-free reference of the same material. The irreversible length change caused by removal of open volume defects (e.g. vacancies) is obtained from comparison of the length change of the sample studied and defect-free reference upon annealing. The sample volume change calculated from irreversible length change determined by time dependent differential dilatometry of HPT-deformed Fe, Cu and Ni exceeds significantly the volume change expected from recovery of dislocations and relaxation of grain boundaries.[30,33] This indicates that a high portion of excess free volume in HPT-deformed metals is comprised of vacancies.[29] The absolute concentration of vacancies determined in HPT-deformed Ni by the time dependent differential dilatometry was in the range $(4–7) \times 10^{-4}$.[34] This again testifies to a high concentration of vacancies introduced by SPD.

Hence, it is clear that vacancies play an important role in SPD processing and detailed knowledge about the formation of vacancies by SPD and their development during SPD processing is highly desirable. The importance of deformation-induced vacancies is demonstrated by enhanced diffusion processes in UFG materials, e.g. re-ordering of intermetalic compounds,[35,36] precipitation effects,[37–39] solid state reactions in alloys[16,40] and solute segregation.[41–43]

Positron annihilation spectroscopy (PAS)[44,45] is an excellent tool for investigations of vacancies in solids. PAS is a non-destructive technique with a very high sensitivity to vacancies ($\sim 10^{-6}$ at.$^{-1}$). Positron, i.e. an antiparticle of electron, is used as a probe in the lattice of samples studied. Positrons are obtained usually from β^+ radioisotopes prepared by bombarding of suitable target by protons in a cyclotron. A ^{22}Na radioisotope with the half-lifetime of 2.6 year is used most frequently as a positron source. A gamma ray with the energy of 1274 keV – so called start signal – is emitted practically simultaneously with positron due to de-excitation of the daughter ^{22}Ne nucleus. Energetic positrons implanted into a solid are thermalized within a few ps, i.e. their kinetic energy decreases down to a fraction of eV, and diffuse throughout the lattice until they are annihilated by one of the surrounding electrons. The annihilating electron-positron pair is converted into two gamma rays with the energy of 511 keV which can be detected by scintillation detectors. The time difference between the start signal emission and the annihilation gamma ray appearance defines the lifetime of each positron. Hence, the positron lifetime (LT) is an observable related to positron annihilation process and a measure of electron density felt by positron in the lattice. In a perfect (defect-free) lattice positron is delocalized in a Bloch-like state and positron density can be described by a modulated plane wave. If open volume defects, e.g. vacancies, dislocations etc., are present in the sample positron can be trapped at one of these defects and its density becomes confined in the defect. Since local electron density in open volume defects is lower compared to a perfect lattice, trapped positrons live longer. The lifetime of trapped positrons is a measure of the open volume in each type of defects. As an example Fig. 1 shows the calculated positron density for a delocalized positron (perfect lattice, lifetime $\tau_B = 114$ ps), a

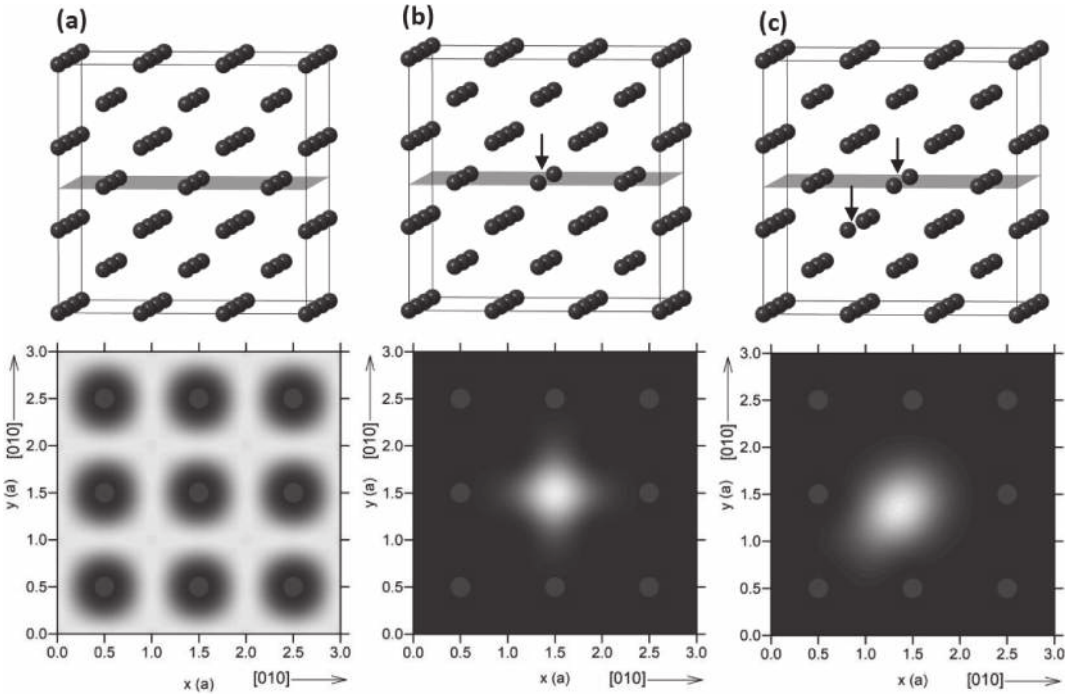

Fig. 1 Calculated positron density in the (002) plane in fcc Cu: (a) positron delocalized in a perfect lattice; (b) positron trapped in mono-vacancy; (c) positron trapped in di-vacancy. Positron density was calculated in a $3 \times 3 \times 3$ supercell. Positions of vacancies are indicated by arrows.

positron trapped in a mono-vacancy (lifetime $\tau_{1V} = 180$ ps), and a positron trapped in a di-vacancy (lifetime $\tau_{2V} = 204$ ps) in Cu.[46] Hence LT spectroscopy enables identification of open volume defects in samples studied.

A non-zero momentum of annihilating electron–positron pairs leads to a Doppler shift in the energy of annihilation radiation. The momentum of the thermalized positron is negligible compared to that of electron. Hence, the Doppler shift of annihilation radiation carries information about the momentum distribution of the electrons which annihilated positrons. The Doppler shift causes a broadening of the annihilation photopeak in the gamma ray energy spectrum, which can be analyzed using so-called *S* (sharpness) line-shape parameter which is defined as the central area of the annihilation photo-peak divided by the net peak area,[44,45] see Fig. 2. The *S* parameter is a measure of the contribution of positrons annihilated by low-momentum electrons. When a positron is trapped at an open volume defect, its wave function becomes localized in the defect, which leads to a reduction of its overlap with high-momentum core electrons and narrowing of the annihilation photopeak. As a consequence, the S parameter increases. The main advantage of the Doppler broadening (DB) technique is that the measurement is relatively fast. While the measurement of a LT spectrum with sufficient statistics of 10^7 annihilation events takes at least 1 day using a standard positron source, a single DB spectrum can be acquired within ≈30 min.

PAS has been extensively used for the investigation of open volume defects (vacancies, vacancy clusters, dislocations, grain boundaries etc.) in solids for more than 50 years. The state-of-art of PAS investigations of defect in metals was described in the recent review.[47] In particular PAS has been successfully employed for investigations of vacancies introduced into UFG materials by SPD.[11–14,46–51]

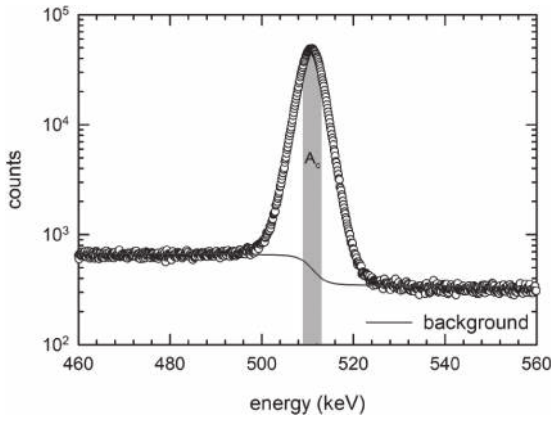

Fig. 2 A schematic illustration of the positron annihilation photo-peak. The *S* parameter is defined as the ratio of the central area of the annihilation peak A_c (filled by grey colour) and the net peak area. The solid line shows the background which is subtracted prior to calculation of the *S* parameter.

2. Experimental Details

Pure metals (Mg, Al, Ti, Fe, Ni, Cu, Nb, W) were deformed by HPT at room temperature in quasi-constraint condition[4] using a pressure of 6 GPa. HPT-deformed specimens were disc shaped with the thickness of ≈0.3 mm and the diameter of ≈9 mm. In order to study the structural evolution and fragmentation during the HPT processing samples strained by various numbers of revolutions *N* were prepared.

Microstructure of UFG samples was characterized by TEM carried out on a JEOL JEM 2000FX microscope operating at 200 kV. Thin foils for TEM were prepared by electrolytical twin-jet polishing.

A ^{22}Na radioisotope with the activity of 1 MBq deposited on a 2 μm thick mylar foil was used as a positron source for

PAS investigations. The diameter of the positron source spot was approximately 3 mm. A digital spectrometer described in Ref. 52) was employed for LT measurements. The spectrometer exhibits the time resolution of 145 ps (full width at half maximum of the resolution function). At least 10^7 positron annihilation events were accumulated in each LT spectrum. Decomposition of LT spectra into exponential components was performed using a maximum likelihood-based code.[53)]

Some fraction of positrons is annihilated in the source itself. This so called source contributions was determined using a well annealed Fe reference sample which contains negligible concentration of defects and virtually all positrons are annihilated in the free state characterized by the bulk lifetime of 107 ps.[52)] The source contribution consists of a component with lifetime of 368 ps representing a contribution of positrons annihilated in the source spot and a long lived component with lifetime of 1.1 ns originating of pick-off annihilation of ortho-positronium[55)] formed in 2 μm thick mylar foil covering the source.[54)] The intensity of the source contribution depends on the Z number of the sample since certain fraction of positrons entering the sample is scattered back to the source.[56)] The probability of backscattering increases with increasing Z number of the sample.[57)] Hence, the source contribution intensity was recalculated for each sample according to its Z number using the procedure described in Ref. 58). The intensity of the source contribution in the samples studied fall into the range from 6.4% (for Mg) to 11.0% (for W). In decomposition of LT spectra the source contribution was kept fixed at the values known from the reference sample.

The LT measurements were performed (i) in the central region of the sample disc, i.e. positron source was centered in the center of the sample and the region located in the radial distance from the center $r < 1.5$ mm was probed, and (ii) in the periphery with positron source placed at the radial distance $r = 3.0$ mm, i.e. the region in the radial distance $1.5 < r < 4.5$ mm was probed.

The DB spectroscopy was performed using a HPGe detector with energy resolution of 1.0 keV at the annihilation photo-peak energy of 511 keV. The central region for calculation of the S parameter was chosen symmetrically around the 511 keV annihilation peak from 510.16 to 511.84 keV. The S values were normalized to the S parameter S_0 measured in a well annealed material. A ^{22}Na positron source with activity of 0.5 MBq was used for DB measurements. The source spot was carefully deposited on a 2 μm mylar foil so that the spot diameter was smaller than 1 mm. DB measurements were performed on a perpendicular grid with incremental spacing of 1.0 mm by placing the positron source spot at various nodes of the grid using a micrometer x–y shift.

3. Theoretical Calculations

Theoretical calculations of positron lifetimes were performed within the so-called standard scheme[59)] employing the atomic superimposition method for the construction of electron density.[60)] The electron–positron correlation effects were treated using the exchange-correlation potential and enhancement factor introduced by Boroński and Nieminen.[61)] The calculations were done in 500 atom-based supercells for fcc metals and 250 atom-based supercells for bcc and hcp metals. Vacancies and vacancy clusters were introduced by removing the corresponding number of atoms from the supercell. Equilibrium geometry of vacancy clusters was obtained by minimizing their surface. No atomic relaxations were considered in the present stage of calculations.

4. Results and Discussion

4.1 Comparison of various UFG metals prepared by HPT

Table 1 shows lifetimes and relative intensities resolved in LT spectra of UFG metals prepared by HPT using $N = 5$. The PAS measurements were performed in the central region of the sample disk ($r < 1.5$ mm), see Ref. 62) for more details.

The LT spectra of HPT-deformed metals contain in general up to three components. The first short-lived component with lifetime τ_1 represents a contribution of free positrons not trapped at defects. This component is present only in HPT deformed Mg and Al. The presence of the free positron component indicates that dynamic recovery of UFG structure occurred already during HPT processing. Indeed, TEM micrograph in Fig. 3(a) shows that HPT-deformed Mg

Table 1 Lifetimes and relative intensities of exponential components resolved in LT spectra of UFG metals prepared by HPT using $N = 5$ revolutions.[62)] PAS measurements were performed in the central region of the sample disk. The average number of vacancies n_{vac} contained in vacancy clusters and the width w_{vac} (full width at half maximum) of the size distribution of vacancy clusters are given in the last two columns. Uncertainties (one standard deviation) expressed in the units of the last significant digit are shown in the parentheses.

Sample	Structure	τ_1 (ps)	I_1 (%)	τ_2 (ps)	I_2 (%)	τ_3 (ps)	I_3 (%)	n_{vac}	w_{vac}
Mg	hcp	188(5)	39(1)	257(3)	61(1)	-	-	-	-
Al	fcc	149(8)	71(5)	252(9)	26(1)	450(50)	3(1)	40(4)	15
Ti	hcp	-	-	185.2(5)	98.4(7)	430(70)	1.6(7)	50(6)	17
Fe	bcc	-	-	150.8(6)	91.1(4)	360(9)	8.9(4)	13.1(5)	8
Ni	fcc	-	-	157(1)	88(1)	336(8)	12(1)	14.3(6)	9
Cu	fcc	-	-	164(1)	76.0(6)	256(2)	24.0(5)	4.0(3)	4
Nb	bcc	-	-	173.9(8)	94(1)	300(10)	6(1)	3.9(2)	4
W	bcc	-	-	160.8(6)	90.8(4)	367(7)	9.2(7)	13(1)	8

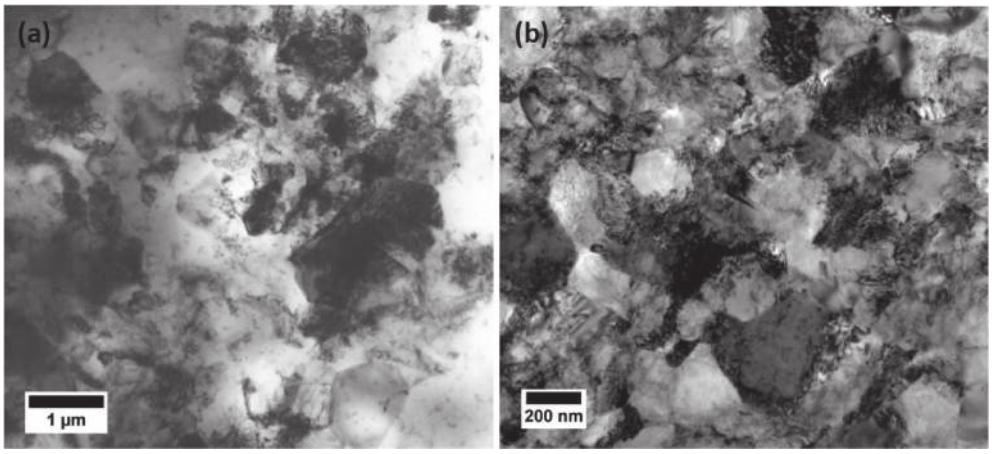

Fig. 3 Bright field TEM micrographs of (a) HPT deformed Mg; (b) HPT deformed Cu.

exhibits the bimodal structure consisting of UFG regions with grain size of 100–300 nm and recrystallized regions with coarse grains of 1–10 μm in diameter. Similar kind of bimodal structure was observed in HPT deformed Al. Dynamic recovery in Mg and Al is obviously a consequence of a high mobility of dislocations at room temperature considering relatively low melting temperature T_m of both Mg and Al. Room temperature (300 K) corresponds to 0.33 T_m and 0.32 T_m for Mg and Al, respectively. Moreover, since both Mg and Al have relatively high stacking fault energy, dislocations are not split into partial, which has a positive impact on their mobility. In contrast to Mg and Al no free positron component was resolved in other HPT deformed metals studied. It indicates that defect density in other UFG metals is so high that all positrons are annihilated in trapped state at defects.

The second component with lifetime τ_2 comes from positrons trapped at dislocations. Positron trapping at dislocations is a two-state process.[63] The dislocation line itself is only a shallow positron trap. Positron weakly localized in a dislocation diffuses quickly along the dislocation line until it becomes finally confined at a deep trap provided by a vacancy anchored in the compressive elastic field of the dislocation.[63] Hence, positron is finally annihilated in a vacancy squeezed by the compressive elastic field of the dislocation which results in a lifetime slightly shorter than the lifetime of positrons trapped in a monovacancy.[46] The dislocation component exhibits a dominating intensity in all samples studied, except for HPT deformed Al where a pronounced recovery of dislocations occurred, see Table 1. Hence, dislocations are dominating positron traps in HPT deformed metals. This can be easily understood considering that the dislocation is a line defect with a single macroscopic dimension. As a consequence, the cross-section for positron trapping at dislocations is significantly higher than that for point defects. Figure 3(b) shows the microstructure of HPT deformed Cu as an example of the UFG structure with grain size around 100 nm where no dynamic recovery occurred. A high density of dislocations arranged into a cellular structure is clearly seen in the micrograph. This is typical for cubic metals with a high and medium stacking fault energy. Similar microstructure was observed in HPT deformed Ni, Fe, Nb and W.

A long-lived component exhibits the lifetime τ_3 which is significantly longer than the lifetime of a monovacancy in a given material. This component can be attributed to positrons trapped at vacancy clusters. The component from vacancy clusters was observed in all HPT-deformed metals studied. The only exception is HPT deformed Mg. Dynamic recovery of UFG structure occurs both in Mg and Al. But the difference between these two materials is based on the fact that dislocations in Al form a cellular sub-structure while in Mg dislocations are distributed uniformly inside grains due to a limited number of active slip systems. Uniform spatial distribution of dislocations facilitates the recovery of deformation-induced vacancies which can easily diffuse along dislocations to sinks at grain boundaries. As a consequence, in HPT-deformed Mg almost all deformation-induced vacancies were recovered while in HPT deformed Al some fraction of vacancies agglomerated into vacancy clusters.

The mean size of vacancy clusters can be estimated by comparison of the lifetime τ_3 with theoretical calculations of positron lifetimes for vacancy clusters consisting of various numbers of vacancies.[62] Figure 4 shows results of such calculations for selected metals with fcc, bcc and hcp structure. Obviously the lifetime of trapped positrons increases with increasing open volume of vacancy cluster and gradually saturates for vacancy clusters consisting of more than ≈50 vacancies. The comparison of experimentally measured lifetime τ_3 with results of theoretical modelling allows us to determine the average size of vacancy clusters in UFG materials. The average number of vacancies n_{vac} in vacancy clusters formed in various HPT-deformed metals is listed in the last column of Table 1. It is obvious that a certain size distribution of vacancy clusters is established in HPT-deformed metals. It was reported that the size distribution of vacancy clusters can be well described by Poisson distribution.[62] The width of the size distribution (full width at half maximum) is given in the last column of Table 1. The agglomeration of deformation-induced vacancies is influenced by the mobility of vacancies. Large clusters observed in Al and Ti were likely formed due to rather low activation energy E_m for migration of vacancies in these two metals. Theoretical calculations revealed that the vacancy migration energy for Ti and Al is 0.43 eV[64] and 0.42 eV,[65] respectively.

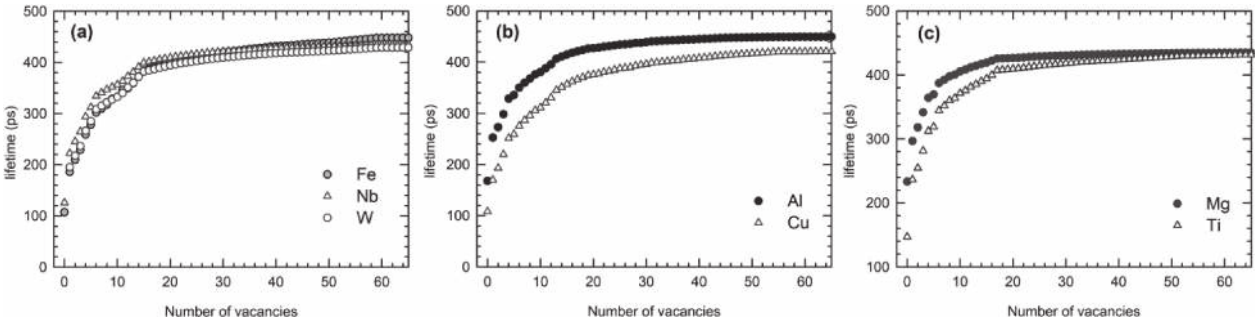

Fig. 4 Calculated lifetimes of positrons trapped at vacancy clusters plotted as a function of the number of vacancies in the cluster: (a) bcc metals; (b) fcc metals; (c) hcp metals.[62]

These migration energies are less than half of the value for Cu ($E_m = 1.00$ eV).[66]

Vacancy clusters were created by agglomeration of vacancies introduced by SPD. Climbing of dislocations and motion of screw dislocations with jogs having edge character introduce chains of vacancies or interstitial atoms. Creation of vacancies dominates because vacancies have lower formation energy than interstitials. In most metals studied in the present work vacancies are mobile at room temperature. Some fraction of deformation-induced vacancies, therefore, disappears by diffusion to sinks at grain boundaries and the surface while vacancies which agglomerate into vacancy clusters remain in the sample. The driving force for agglomeration of vacancies is the reduction of the surface energy and this process is facilitated by the fact that vacancies are created in chains, i.e. close to each other. Note that contrary to metals prepared by SPD vacancy clusters are usually not observed in conventionally deformed metals, e.g. by cold rolling. It indicates that SPD introduces significantly higher number of vacancies than conventional plastic deformation.

4.2 Concentration of deformation-induced vacancies

High density of defects in UFG samples prepared by SPD results in saturated positron trapping, i.e. the concentration of defects is so high that virtually all positrons are annihilated in trapped state at defects. Saturated positron trapping prevents determination of absolute concentration of defects from PAS data. From analysis of PAS data one obtains only concentration ratio of defects present in the UFG sample, i.e. vacancy clusters and dislocations. In order to get absolute concentration of vacancy clusters the dislocation density has to be determined independently by some other method, e.g. by X-ray diffraction.

Detailed analysis of the concentration of vacancies introduced by SPD was performed in Cu deformed by HPT by combining of PAS and XLPA investigations.[67] The concentration of deformation-induced vacancies in HPT-deformed Cu increases with strain from $c_v \approx 0.4 \times 10^{-3}$ at.$^{-1}$ for $\gamma \approx 18$ ($N = 1$, $r = 1.5$ mm) up to 2×10^{-3} at.$^{-1}$ for $\gamma \approx 780$ ($N = 25$, $r = 3.0$ mm).[67] This range is consistent with the concentrations of vacancies estimated in UFG Cu samples by Ungár *et al.*[21]

Some part of the plastic work applied to a strained material is spent for the generation of dislocations and other part for the creation of vacancies. Hence, the total concentration of vacancies c_{total} introduced by plastic deformation is proportional the plastic work[68]

$$c_{total} \approx \frac{W_v}{G} \int_0^{\gamma} \tau \, d\gamma, \tag{2}$$

where τ is the shear stress, γ is the strain, G is the shear modulus, and the coefficient $W_v \sim 10^{-2}$[69] represents the fraction of plastic work stored in vacancies. The shear stress is $\tau = \frac{F}{A}$, where F is the shear force and $A = \pi R^2$ is the area of disk sample with radius R. Inserting eq. (1) into (2) one gets an estimation of the total concentration of vacancies introduced by HPT into a region in the radial distance r from the centre of the sample[67]

$$c_{total} \approx \frac{W_v}{G} \frac{4Fr^3}{hR^4} N. \tag{3}$$

The total concentration of deformation-induced vacancies c_{total} in the distance $r = 3$ mm from the centre calculated by eq. (3) for a HPT deformed Cu sample with the thickness $h = 0.3$ mm and radius $R = 4.5$ mm is plotted in Fig. 5 as a function of the number of revolutions. The shear modulus of Cu $G = 48.3$ GPa[70] and the torque of $\approx$5 Nm[67] corresponding to the shear force of $\approx$1.1 kN at the periphery of the sample were considered in the calculation. In Fig. 5 the total

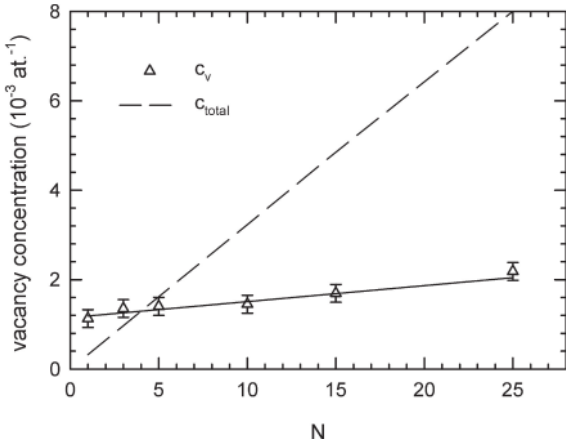

Fig. 5 The concentration of vacancies c_v in HPT deformed Cu subjected to various numbers N of HPT revolutions. The concentration of vacancies was determined in the distance $r = 3$ mm from centre of the sample disk by combining PAS and XLPA data.[67] The total concentration of deformation induced vacancies c_{total} calculated by eq. (3) is plotted in the figure as well.

concentration of deformation-induced vacancies is compared with the actual concentration of vacancies determined in the sample by combining PAS and XLPA data.[67] The concentration of vacancies which survived in the HPT-deformed sample represents 40–50% of the net concentration of deformation induced vacancies (i.e. $c_v/c_{total} \approx 0.4$–$0.5$). Hence at least 50% of vacancies introduced by SPD into Cu disappeared by diffusion to sinks at grain boundaries. The fraction of vacancies lost by diffusion to sinks increases with increasing number of revolutions since the density of sinks increases as the grain refinement proceeds. Remaining vacancies which did not disappear in sinks agglomerated into vacancy clusters which persist in the sample and were detected by PAS.

4.3 Spatial distribution of vacancies

Owing to the non-uniform distribution of strain in HPT deformed sample expressed by eq. (1) the homogeneity of UFG structure of materials deformed by HPT has been extensively studied.[7–11] Vickers microhardness (HV) measured in a regular mesh across the sample is a simple and feasible technique for mapping of the homogeneity of UFG structure. For this reasons HV mapping has been frequently employed to study the stress distribution of HPT deformed samples.[7–11] In most materials the development of HV across the sample is similar to that for HPT-deformed Cu plotted in Figs. 6(a)–(c). From inspection of the figure it is clear that HV pattern has the axial symmetry and is governed only by the radial distance r from the centre of the sample. In early stages of HPT processing HV increases first in the edge of the sample, i.e. in the region with the highest imposed strain, while HV in the central region is significantly lower, see Fig. 6(a). With increasing number of revolutions the strengthened region with enhanced HV gradually extends toward the centre, see Fig. 6(b). Finally after sufficient number of revolutions HV becomes almost uniform across the whole sample, see Fig. 6(c). HV mapping is a versatile tool for study of the homogeneity of UFG structure. It is sensitive to dislocation density ρ_D through work hardening which obeys the relation HV $\sim \sqrt{\rho_D}$[71] and grain refinement via grain boundary hardening governed by the Hall-Petch relation HV $\sim 1/\sqrt{d}$,[72] where d is the mean grain size. Hence, HV map provides information about grain refinement and dislocation density across the sample but no information about spatial distribution of vacancies since hardening caused by vacancies is usually too small to be detectable by HV testing.

Information about spatial distribution of vacancies in UFG materials deformed by HPT can be obtained by PAS, namely by employing the DB spectroscopy.[11] Figures 6(d)–(f) show colour coded maps of HPT deformed Cu[11] created using the S line shape parameter which is a measure of the fraction of positrons annihilated by low momentum valence/conductive electrons. From inspection of Fig. 6 one can conclude that DB maps are axially symmetric similarly to HV ones, but the radial dependence of the S parameter differs from that of HV. The S parameter is remarkably enhanced in the periphery and remains lower in the central region. With increasing number of HPT revolutions S increases also in the central region but in contrast to HV the difference between the centre and the periphery is pronounced even after 25 HPT revolutions, cf. Fig. 6(c) and (f).

LT investigations indicate that positrons in UFG Cu samples are trapped either at dislocations or in vacancy

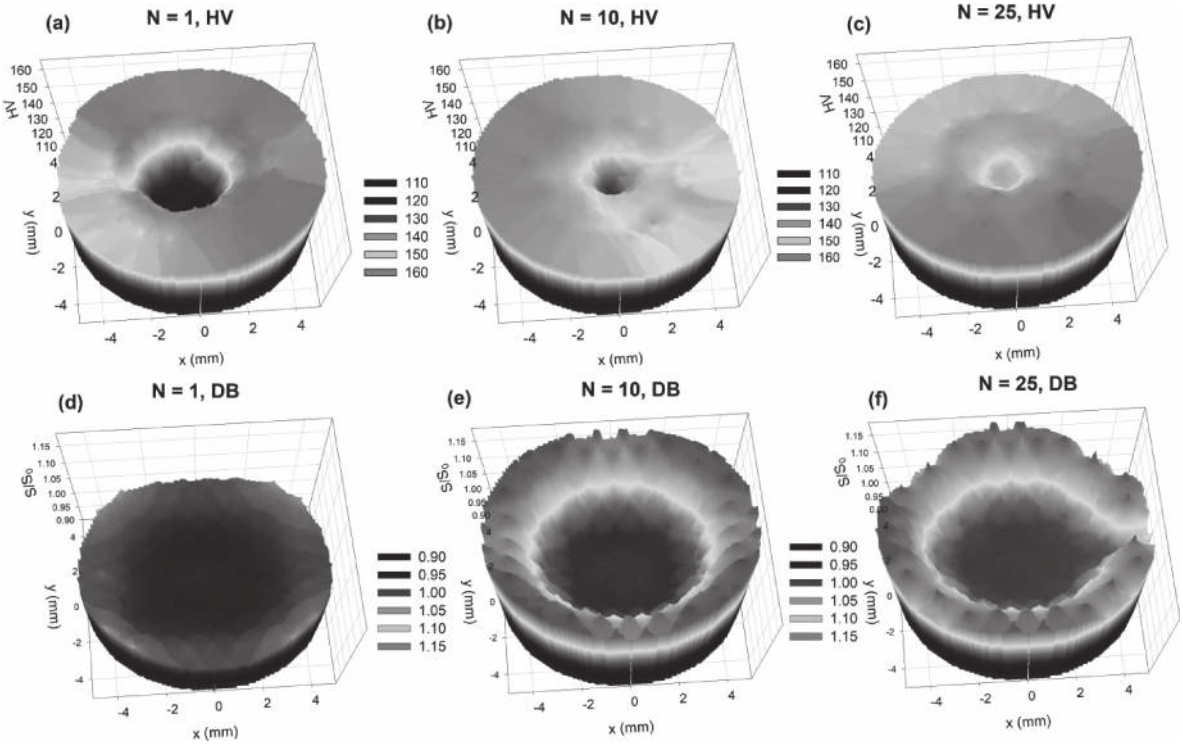

Fig. 6 UFG Cu subjected 1, 10 and 25 HPT revolutions: colour coded map of (a), (b), (c) microhardness (HV); (d), (e), (f) S-parameter determined from Doppler broadening of the annihilation photo-peak. The S parameter values were normalized to the value S_0 corresponding to a well annealed Cu.[11]

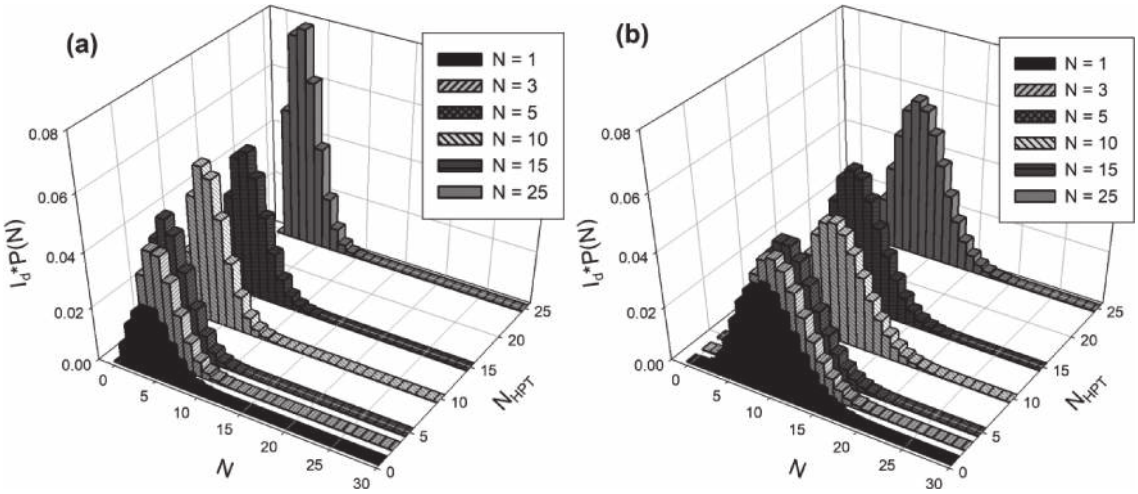

Fig. 7 The size distribution of vacancy clusters in UFG Cu deformed by HPT for different numbers of revolutions N: (a) central region of the sample, $r < 1.5$ mm; (b) periphery of the sample, $r = 3.0$ mm. The size distribution of vacancy clusters P(n_{vac}) was determined by PAS using the approach described in Ref. 62). The size distribution of vacancy clusters in the figure was multiplied by the intensity I_{cl} of positrons trapped at vacancy clusters which is a measure of the concentration of vacancy clusters.[62)]

clusters. Since HV map demonstrates that the density of dislocations becomes uniform after sufficient number of HPT revolutions $N \geq 10$, the enhanced S parameter in the periphery of the sample is predominantly caused by vacancies. Hence, DB mapping proved that contrary to dislocations spatial distribution of vacancies is non-uniform even after a high number of revolutions.

A non-uniform distribution of vacancy clusters was confirmed by LT investigations of HPT deformed Cu performed in central region ($r < 1.5$ mm) and at the periphery $r = 3.0$ mm. Figure 7 shows the size distribution of vacancy clusters determined from LT data using the approach described in Ref. 62) assuming that the number of vacancies constituting clusters follows the Poisson distribution. The average size of vacancy clusters in the periphery is obviously higher (i.e. they contain more vacancies) than that of clusters in the centre. Since bigger vacancy clusters are characterized by higher S parameter, the increase of S with r observed in Fig. 6 is caused by the increasing size of vacancy clusters. The size distribution of vacancy clusters in Fig. 7 was multiplied by the intensity I_{cl} of the component which comes from positrons trapped at vacancy clusters. The intensity I_{cl} is a measure of the concentration of vacancy clusters. One can see in Fig. 7 that with increasing number of revolutions I_{cl} increases. It results in a higher area of the size distributions as can be seen in the figure. Thus, the concentration of vacancy increases with increasing number of revolutions but the shape of the size distribution in the central region (the narrower size distribution, the smaller mean size) and in the periphery (the broader size distribution, the higher mean size) remains unchanged.

Increasing size of vacancy clusters with r is connected with the strain rate which in the torsion straining increases with the radial distance r from centre of the sample. The vacancy production rate Π during plastic deformation is proportional to applied stress σ and to the strain rate $\dot{\varepsilon}$ as follows[73)]

$$\Pi = \alpha \frac{\sigma \Omega_0}{E_f} \dot{\varepsilon}. \quad (4)$$

The symbol Ω_0 denotes the atomic volume, E_f is the vacancy formation energy and the coefficient $\alpha \approx 0.1$.[74)] The production rate of vacancies is higher at the periphery than in the centre due to the higher straining rate. Thus, the number of vacancies introduced per unit time in the periphery is higher than in the centre. As a consequence, the agglomeration of vacancies in the periphery results in vacancy clusters which are bigger than in the centre. Since vacancy production rate at a given distance r from the centre remains constant during HPT straining (i.e. it does not change with increasing number of HPT revolutions) the difference in the size of vacancy clusters in the central region and in the periphery does not diminish with increasing number of revolutions and persists even in samples strained by a high number of HPT revolutions.

5. Conclusions

A high concentration of vacancies in the order of 10^{-3}–10^{-4} at.$^{-1}$ is introduced into metals by SPD processing using HPT at room temperature. The concentration of vacancies introduced by SPD approaches the concentration close to the melting point of the strained material. A significant fraction of deformation-induced vacancies disappears by diffusion to sinks at grain boundaries. Remaining vacancies agglomerate into vacancy clusters which persist in UFG samples prepared by SPD techniques. The presence of vacancy clusters consisting on average of 4–50 vacancies was confirmed by PAS in metals with fcc, bcc and hcp structure deformed by HPT. The average size of vacancy clusters increases with increasing distance from the centre of the sample due to increasing strain rate leading to a higher production rate of vacancies. As a consequence, the lateral distribution of vacancies across HPT deformed samples remains non-uniform even after a high number of revolutions.

Acknowledgements

Financial support by the Czech Science Agency (project 17-17016S) is highly acknowledged. T.V. acknowledges support by the grant agency of Charles university (project 1506119). Partial financial support by the Ministry of Education Youth and Sports (project LTARF18010) and by ERDF project no. CZ.02.1.01/0.0/0.0/15 003/0000485 is also gratefully acknowledged.

REFERENCES

1) R.Z. Valiev, Y. Estrin, Z. Horita, T.G. Langdon, M.J. Zehetbauer and Y.T. Zhu: JOM **58** (2006) 33–39.
2) R.Z. Valiev, R.K. Islamgaliev and I.V. Alexandrov: Prog. Mater. Sci. **45** (2000) 103–189.
3) R.N. Harsha, V. Mithun Kulkarni and B. Satish Babu: Mater. Today: Proc. **5** (2018) 22340–22349.
4) A.P. Zhilyaev and T.G. Langdon: Prog. Mater. Sci. **53** (2008) 893–979.
5) R. Pippan, S. Scheriau, A. Taylor, M. Hafok, A. Hohenwarter and A. Bachmaier: Annu. Rev. Mater. Res. **40** (2010) 319–343.
6) K. Edalati and Z. Horita: Mater. Sci. Eng. A **652** (2016) 325–352.
7) A.P. Zhilyaev, G.V. Nurislamova, B.K. Kim, M.D. Baro, J.A. Szpunar and T.G. Langdon: Acta Mater. **51** (2003) 753–765.
8) A.P. Zhilyaev, K. Oh-ishi, T.G. Langdon and T.R. McNelley: Mater. Sci. Eng. A **410–411** (2005) 277–280.
9) Y. Estrin, A. Molotnikov, C.H.J. Davies and R.J. Lapovok: J. Mech. Phys. Solids **56** (2008) 1186–1202.
10) Y.Z. Tian, X.H. An, S.D. Wu, Z.F. Zhang, R.B. Figueiredo, N. Gaob and T.G. Langdon: Scr. Mater. **63** (2010) 65–68.
11) J. Čížek, O. Melikhova, M. Janeček, O. Srba, Z. Barnovská, I. Procházka and S. Dobatkin: Scr. Mater. **65** (2011) 171–174.
12) J. Čížek, P. Hruška, T. Vlasák, M. Vlček, M. Janeček, P. Minárik, T. Krajňák, M. Šlapáková, M. Dopita, R. Kužel, T. Kmječ, J.G. Kim and H.-S. Kim: Mater. Sci. Eng. A **704** (2017) 181–191.
13) J. Čížek, M. Janeček, T. Krajňák, J. Stráská, P. Hruška, J. Gubicza and H.S. Kim: Acta Mater. **105** (2016) 258–272.
14) J. Čížek, P. Haušild, M. Cieslar, O. Melikhova, T. Vlasák, M. Janeček, R. Král, P. Harcuba, F. Lukáč, J. Zýka, J. Málek, J. Moon and H.S. Kim: J. Alloys Compd. **768** (2018) 924–937.
15) A. Hoffman, H. Wen, R. Islamgaliev and R. Valiev: Mater. Lett. **243** (2019) 116–119.
16) K. Oh-ishi, K. Edalati, H.S. Kim, K. Hono and Z. Horita: Acta Mater. **61** (2013) 3482–3489.
17) M. Kocer, F. Sachslehner, M. Müller, E. Schafler and M. Zehetbauer: Mater. Sci. Forum **210–213** (1996) 133–140.
18) D. Setman, E. Schafler, E. Korznikova and M.J. Zehetbauer: Mater. Sci. Eng. A **493** (2008) 116–122.
19) M. Krystian, D. Setman, B. Mingler, G. Krexner and M.J. Zehetbauer: Scr. Mater. **62** (2010) 49–52.
20) M. El-Tahawy, Y. Huang, T. Um, H. Choe, J.L. Lábára, T.G. Langdon and J. Gubicza: J. Mater. Technol. **6** (2017) 339–347.
21) T. Ungár, E. Schafler, P. Hanák, S. Bernstorff and M.J. Zehetbauer: Mater. Sci. Eng. A **462** (2007) 398–401.
22) T. Ungár, E. Schafler, P. Hanák, S. Bernstorff and M. Zehetbauer: Z. Metallk. **96** (2005) 578–583.
23) E. Schafler, G. Steiner, E. Korznikova, M. Kerber and M.J. Zehetbauer: Mater. Sci. Eng. A **410–411** (2005) 169–173.
24) M.J. Zehetbauer, J. Kohout, E. Schafler, F. Sachslehner and A. Dubravina: J. Alloys Compd. **378** (2004) 329–334.
25) W. Sprengel, B. Oberdorfer, E. Steyskal and R. Würschum: J. Mater. Sci. **47** (2012) 7921.
26) R.O. Simmons and R.W. Balluffi: Phys. Rev. **125** (1962) 862.
27) E. Bauerle and J.S. Koehler: Phys. Rev. **107** (1957) 1493.
28) J. Takamura: Acta Metall. **9** (1961) 547–557.
29) R. Würschum, B. Oberdorfer, E.-M. Steyskal, W. Sprengel, W. Puff, P. Pikart, C. Hugenschmidt and R. Pippan: Physica B **407** (2012) 2670–2675.
30) B. Oberdorfer, B. Lorenzoni, K. Unger, W. Sprengel, M. Zehetbauer, R. Pippan and R. Würschum: Scr. Mater. **63** (2010) 452–455.
31) G. Reglitz, B. Oberdorfer, N. Fleischmann, J.A. Kotzurek, S.V. Divinski, W. Sprengel, G. Wilde and R. Würschum: Acta Mater. **103** (2016) 396–406.
32) R. Enzinger, Chr. Neubauer, J. Kotzurek, W. Sprengel and R. Würschum: J. Mater. Sci. **53** (2018) 2758–2765.
33) B. Oberdorfer, D. Setman, E.-M. Steyskal, A. Hohenwarter, W. Sprengel, M. Zehetbauer, R. Pippan and R. Würschum: Acta Mater. **68** (2014) 189–195.
34) J.A. Kotzurek, E.-M. Steyska, B. Oberdorfer, A. Hohenwarter, R. Pippan, W. Sprengel and R. Würschum: Appl. Phys. Lett. **109** (2016) 021906.
35) M. Kawasaki, B. Ahn, H. Lee, A.P. Zhilyaev and T.G. Langdon: J. Mater. Res. **31** (2016) 88–99.
36) C. Gammer, C. Mangler, H.P. Karnthaler and C. Rentenberger: Scr. Mater. **156** (2018) 90–94.
37) M. Hibino, C. Watanabe, Y. Tsuji, R. Monzen, Y. Todaka and W. Sato: Mater. Trans. **58** (2017) 1346–1350.
38) L. Jiang, J.K. Li, G. Liu, R.H. Wang, B.A. Chen, J.Y. Zhang, J. Sun, M.X. Yang, G. Yang, J. Yang and X.Z. Cao: Mater. Sci. Eng. A **637** (2015) 139–154.
39) Y. Chen, N. Gao, G. Sha, S.P. Ringer and M.J. Starink: Mater. Sci. Eng. A **627** (2015) 10–20.
40) Z. Zhang, J. Guo, G. Dehm and R. Pippan: Acta Mater. **138** (2017) 42–51.
41) C. Borchers and R. Kirchheim: Prog. Mater. Sci. **82** (2016) 405–444.
42) Y. Ivanisenko, X. Sauvage, A. Mazilkin, A. Kilmametov, J.A. Beach and B.B. Straumal: Adv. Eng. Mater. **20** (2018) 1800443.
43) A. Hoffman, H. Wen, R. Islamgaliev and R. Valiev: Mater. Lett. **243** (2019) 116–119.
44) P. Hautojärvi: *Positrons in Solids*, (Springer-Verlag, Berlin, 1979).
45) R. Krause-Rehberg and H.S. Leipner: *Positron Annihilation in Semiconductors*, Vol. 127 of Springer Series in Solid-state Sciences, (Springer-Verlag, Berlin, 1999).
46) J. Čížek, I. Procházka, M. Cieslar, R. Kužel, J. Kuriplach, F. Chmelík, I. Stulíková, F. Bečvář and O. Melikhova: Phys. Rev. B **65** (2002) 094106.
47) J. Čížek: J. Mater. Sci. Technol. **34** (2018) 577–598.
48) W. Lechner, W. Puff, B. Mingler, M.J. Zehetbauer and R. Würschum: Scr. Mater. **61** (2009) 383–386.
49) B. Oberdorfer, E.-M. Steyskal, W. Sprengel, W. Puff, P. Pikart, Ch. Hugenschmidt, M. Zehetbauer, R. Pippan and R. Würschum: Phys. Rev. Lett. **105** (2010) 146101.
50) J. Čížek, I. Procházka, M. Cieslar, I. Stulíková, F. Chmelík and R.K. Islamgaliev: Phys. Status Solidi A **191** (2002) 391–408.
51) J. Čížek, I. Procházka, G. Brauer, W. Anwand, R. Kužel, M. Cieslar and R.K. Islamgaliev: Phys. Status Solidi A **195** (2003) 335–349.
52) F. Bečvář, J. Čížek, I. Procházka and J. Janotová: Nucl. Instrum. Methods Phys. Res. A **539** (2005) 372–385.
53) I. Procházka, I. Novotný and F. Bečvář: Mater. Sci. Forum **255–257** (1997) 772–774.
54) F. Bečvář, J. Čížek, L. Lešták, I. Novotný, I. Procházka and F. Šebesta: Nucl. Instrum. Methods Phys. Res. A **443** (2000) 557–577.
55) Y.C. Jean, J.D. Van Horn, W.-S. Hung and K.-R. Lee: Macromolecules **46** (2013) 7133–7145.
56) S. McGuire and D.J. Keeble: J. Phys. D **39** (2006) 3388–3393.
57) M. Singh and K.K. Sharma: Jpn. J. Appl. Phys. **26** (1987) 2090–2094.
58) H. Surbeck: Helv. Phys. Acta **50** (1977) 705–721.
59) M.J. Puska and R.M. Nieminen: Rev. Mod. Phys. **66** (1994) 841–897.
60) M.J. Puska and R.M. Nieminen: J. Phys. F **13** (1983) 333–346.
61) E. Boroński and R.M. Nieminen: Phys. Rev. B **34** (1986) 3820–3831.
62) J. Čížek, O. Melikhova, Z. Barnovská, I. Procházka and R.K. Islamgaliev: J. Phys. Conf. Ser. **443** (2013) 012008.
63) L.C. Smedskjaer, M. Manninen and M.J. Fluss: J. Phys. F **10** (1980) 2237–2250.
64) G. Verite, F. Willaime and Ch.-Ch. Fu: Solid State Phenomena **129** (2007) 75–81.
65) A. Da Fano and G. Jacucci: Phys. Rev. Lett. **39** (1977) 950–952.
66) Yu.M. Plishkin and I.E. Podchinenov: Phys. Status Solidi A **38** (1976) 51–55.
67) J. Čížek, M. Janeček, O. Srba, R. Kužel, Z. Barnovská, I. Procházka

and S. Dobatkin: Acta Mater. **59** (2011) 2322–2329.
68) I. Kovacs and L. Zsoldos: *Dislocations and Plastic Deformations*, (Elsevier, Amsterdam, 1973).
69) M. Zehetbauer: Key Eng. Mater. **97–98** (1994) 287–306.
70) F.J. Humphreys and M. Hatherly: *Recrystallization and Related Annealing Phenomena*, (Pergamon Press, Oxford, 2004).
71) G.I. Taylor: Proc. R. Soc. London Ser. A **145** (1934) 362–387.
72) N.J. Petch: Philos. Mag. **3** (1958) 1089–1097.
73) M. Militzer, W.P. Sun and J.J. Jonas: Acta Metall. Mater. **42** (1994) 133–141.
74) G. Gottstein, J. Bewerunge, H. Mecking and H. Wollenberger: Acta Metall. **23** (1975) 641–652.